ACS OMEGA

http://pubs.acs.org/journal/acsodf

Article

WS_2 Nanotube-Embedded SiOC Fibermat Electrodes for Sodium-Ion Batteries

Sonjoy Dey, Krishnappa Manjunath, Alla Zak, and Gurpreet Singh*

Cite This: *ACS Omega* 2023, 8, 10126−10138

Read Online

ACCESS | Metrics & More | Article Recommendations | Supporting Information

ABSTRACT: Layered transition metal dichalcogenides (TMDs) such as tungsten disulfide (WS_2) are promising materials for a wide range of applications, including charge storage in batteries and supercapacitors. Nevertheless, TMD-based electrodes suffer from bottlenecks such as capacity fading at high current densities, voltage hysteresis during the conversion reaction, and polysulfide dissolution. To tame such adverse phenomena, we fabricate composites with WS_2 nanotubes. Herein, we report on the superior electrochemical performance of ceramic composite fibers comprising WS_2 nanotubes (WS_2NTs) embedded in a chemically robust molecular polymer-derived ceramic matrix of silicon-oxycarbide (SiOC). Such a heterogeneous fiber structure was obtained via electrospinning of WS_2NT/preceramic polymer solution followed by pyrolysis at elevated temperatures. The electrode capacity fading in WS_2NTs was curbed by the synergistic effect between WS_2NT and SiOC. As a result, the composite electrode exhibits high initial capacity of 454 mAh g^{-1} and the capacity retention approximately 2-3 times higher than that of the neat WS_2NT electrode.

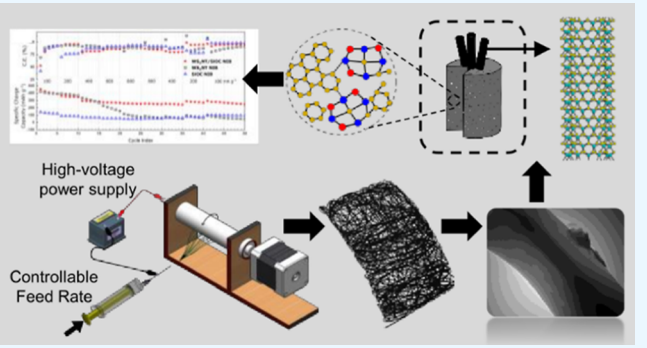

1. INTRODUCTION

The introduction of the heterostructure into the field of energy storage is well appreciated due to various advantageous synergic effects. Unique and composite heterostructures alleviate the bottlenecks of each building block, furnishing the overall property by fine-tuning energy band structures, facilitating ion diffusion kinetics, and perpetuating structural stability.[1] Although two-dimensional (2D) layered materials are efficacious for energy storage applications, new strategies such asusing of rolled-up 2D materials and instigating one-dimensional (1D) nanotubes could bring new initiatives for the scientific community to delve into the kinds of materials for energy storage devices.[2,3] 2D transition metal dichalcogenides (TMDs) possess a sheet-like morphology that consists of covalently bonded chalcogen−metal−chalcogen layers, while the layers are kept together by weak van der Waals (vdW) forces. This unique structure renders them useful for application in fundamental and technological disciplines such as catalysis, energy storage, sensing, and electronic devices.[4] Among the various 2D TMDs, WS_2 has a lamellar structure with an interlayer spacing of 0.62 nm between (002) lattice planes, thus offering suitable space for the reversible insertion of large-sized ions like sodium, for example.[5] Distinctively tailored nanostructured configurations have recently been proposed with WS_2 materials, and their application has been widely explored for electrochemical energy storage devices. Examples include nanoflakes,[6] nanosheets,[7] nanohoneycombs,[8] nanotubes,[9] and nanoflowers[10] of WS_2 to enhance the performance of energy storage devices, specifically lithium-ion batteries (LIBs). Unique structures of WS_2 have rarely been studied for sodium-ion batteries (NIBs).[11,12] Although their counterparts, namely MoS_2 nanotubes, have been extensively studied for electrochemical energy storage, electrochemical hydrogen storage, and used as field effect transistors, up-to-date WS_2 nanotubes (WS_2NTs) have only been studied in LIBs and NIBs to a muchlesser extent, even though they establish stable cycling over a wide voltage range.[9,13,14] Theoretical calculations indicated that single-wall WS_2NTs are an exclusive type of semiconductor with an explicit band gap ranging from 0.1 to 1.9 eV, depending on their diameter.[15,16] They become both direct (in the case of a zigzag) and indirect (in the case of an armchair) band gap semiconductors controlled by chirality, making them useful for various technological applications such as next-generation electronic and optoelectronic devices and high-quality factor nanoelectromechanical systems.[15,17] However, the electronic properties of multiwall WS_2NTs, which are currently produced in large amounts, are not that different from those of the bulk

Received: November 21, 2022
Accepted: February 23, 2023
Published: March 8, 2023

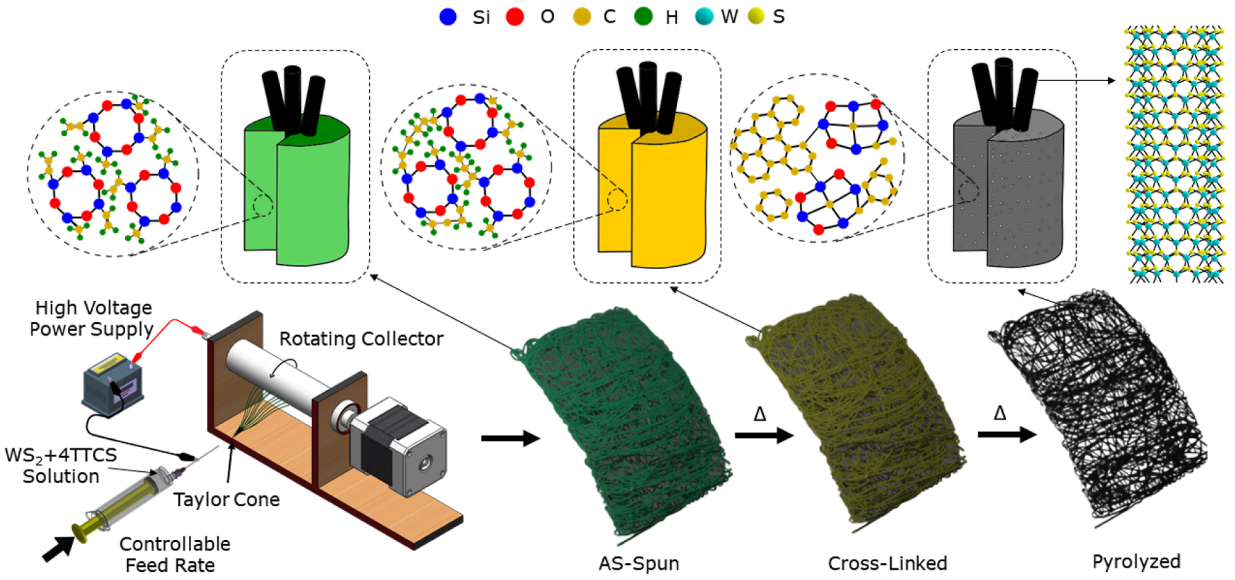

Figure 1. Schematic of the synthesis process of the WS_2NT/SiOC fibermat from electrospinning to cross-linking to pyrolysis steps through controlled annealing. The schematic on top shows the predicted structure of 4TTCS, cross-linked 4TTCS, and the pyrolyzed SiOC structure, along with the WS_2NT structure embedded within the SiOC fibers.

material, that is, having an indirect band gap of ∼1.9 eV.[18] Such a small bandgap make them suitable for the next generation electrochemical energy storage devices.

In spite of its advantageous properties, WS_2 based electrodes suffers from low electronic conductivity, restacking of nanosheets, dissolution of chalcogen species, and significant volume change during repeated charge and discharge cycles.[19] Therefore, hybrid structures that amalgamate conductive carbon networks with the TMDs in which the TMDs provide numerous active sites and channels for alkali metal-ion intercalation, have been widely investigated.[14] Specifically, in rechargeable battery applications, an optimal electrode structure using TMDs should exhibit high electrical conductivity as well as a morphology with sufficient pores and channels to induce the volume change of TMDs. In addition to minimizing secondary reactions originating due to the large surface area of TMDs.[20] For alleviating the aforementioned deleterious properties, heterostructures of WS_2NTs and carbon have been utilized in a recent study, where an improvement in the electrochemical properties of WS_2NTs were observed. The investigation led by Zdeněk and co-workers showed that the NTs-WS_2@C composite electrode sustained a capacity of 152 mA h g^{-1} after 60 cycles when tested at a current density of 80 mA g^{-1} in a sodium ion half-cell.[21] However, such a capacity is insufficient to fulfill the need for application in modern technological devices. An alternative hybridization method to minimize the shortcomings of TMD-based 1D structures is to functionalize them with polymer-derived ceramic materials (PDCs). The rationale behind the functionalization of WS_2NTs with PDCs is that nanotubes possess high mechanical strength , while the carbon network in PDCs can provide a conductive pathway and shorten the ion diffusion route.[22,24]

The primary objectives of this investigation were to exploit the chemical functionalization of 1D WS_2NTs with PDCs and to fabricate a heterogeneous structure of WS_2NTs embeded and wrapped with SiOC fibers. This structure was achieved via a single-step electrospinning process where WS_2NTs and a liquid-phase organosilicon precursor were utilized during solution preparation. The as-fabricated non-woven fibermat was then annealed in a high-temperature pyrolysis environment to obtain the final form that was then characterized via microscopic and spectroscopic techniques to confirm the chemical bonding of the materials. After morphological characterization, the fibermats were tested as working electrode in a sodium-ion half-cell at a gradually increasing current rate. The first-cycle charge capacity of the fabricated composite electrode was 454.05 mA h g^{-1} with a coulombic efficiency exceeding 50%. The composite electrode showed enhanced capacity retention compared with the neat WS_2NTs and SiOC electrodes (2−4 times higher capacity retention in subsequent cycles). This is the first known investigation to report a combination of 1D WS_2NTs within SiOC fibers to create a heterogeneous structure for NIB application.

2. MATERIALS, METHODS, AND CHARACTERIZATIONS

2.1. Fibermat Synthesis Process. The solution preparation is the first step in the electrospinning process. Isopropyl alcohol (IPA) purchased from Fisher Chemical (Lenexa, KS, USA), preceramic silicon oligomer, 1,3,5,7-tetramethyl, 1,3,5,7-tetravinyl cyclotetrasiloxane (4-TTCS) purchased from Gelest (Morrisville, PA, USA), and polyvinylpyrrolidone (PVP) with an average molecular mass of 1,300,000 g mol^{-1} purchased from Sigma-Aldrich (Missouri, MA, USA) were mixed with sonicated WS_2NTs (for 10 min) until a black, homogeneous solution was obtained. The WS_2NTs utilized in this study were prepared by the method described by Zak and co-workers.[23] A small amount (1 wt % of 4TTCS) of dicumyl peroxide purchased from Sigma-Aldrich was also mixed with this solution which worked as a cross-linking agent. The weight ratio of the 4TTCS/IPA was kept at 1:9, and the weight ratio of the WS_2NTs/4TTCS was 1:5. PVP was mixed at a weight ratio of 1:3 with 4TTCS, and an 8.5 mL homogeneous black solution was obtained. As the liquid preceramic silicon oligomer, 4TTCS, possessed a low molecular weight (<500 g mol^{-1}), and a linear organic polymer—PVP—was introduced to ensure that the obtained sol−gel after the solution preparation process qualified for electrospinning viscosity

https://doi.org/10.1021/acsomega.2c07464
ACS Omega 2023, 8, 10126−10138

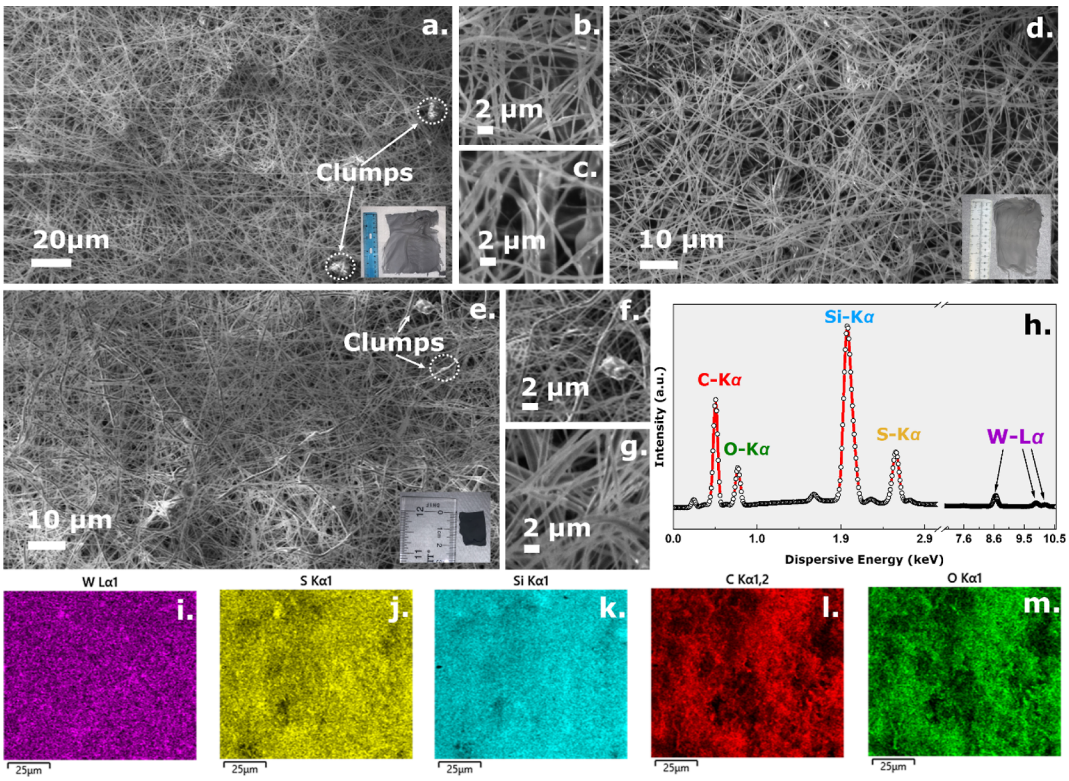

Figure 2. SEM micrograph of the (a) as-spun WS_2NT/SiOC fibermat confirming the fibrous structure of the fibermat; the inset showing the as-spun fibermat digital camera image; (b) magnified portion of figure (a); (c) magnified portion of the cross-linked WS_2NT/SiOC fibermat from figure (d); (d) cross-linked WS_2NT/SiOC fibermat confirming the fibrous structure of the fibermat; the inset indicating the digital camera image of the cross-linked fibermat; (e) pyrolyzed WS_2NT/SiOC fibermat confirming the fibrous structure of the fibermat; the inset showing the digital camera image of the pyrolyzed fibermat; (f,g) magnified portions of the pyrolyzed fibermat showing the agglomeration of some fibers; (h) EDS spectra of the WS_2NT/SiOC fibermat confirming the presence of the materials within; and the corresponding EDS color map for: (i) W-Lα-1; (j) S-Kα-1; (k) Si-Kα-1; (l) C-Kα-1,2; and (m) O-Kα-1.

demands (viscosity should be >10 poise). The flowable and viscous solution was loaded into a syringe with a metallic needle and connected to a high-power voltage source. The other end of the voltage source was connected to a roller collector. With a slow feed rate of 5 mL h^{-1} and the distance between the needle and the roller collector kept at 12 cm, the electrospinning process was initiated with an optimized voltage of 14 kV. As a result, the as-spun fibermat of about 20 × 20 cm^2 was produced, followed by cross-linking the fibermat at 160 °C for 6 h. The final pyrolysis step was carried out in two stages; first, the fibermat was pyrolyzed at 400 °C for 1 h and then at 800 °C for 6 h under an inert argon gas environment. Thus, the black WS_2NT/SiOC fibermat was obtained. The whole fibermat synthesis process is illustrated in Figure 1, showing the electrospinning to cross-linking to the pyrolysis process for obtaining the final fibermat. The predicted structure of SiOC fibers is also illustrated, along with the structure of the WS_2NTs on the same schematic.

2.2. Characterization Techniques. A Carl Zeiss EVO MA10 scanning electron microscope (SEM) was used to obtain SEM micrographs of the fibermats at different stages with a 5−30 kV impinging voltage. A Phillips CM100 transmission electron microscope under an accelerating voltage of 100 kV was used to obtain further insights into the fibrous structure. HORIBA Jobin Yvon LabRam Aramis with a He−Ne laser of wavelength 633 nm and a 17 mW power was used to obtain the Raman spectra of the pyrolyzed fibermat. A 400 FT-IR spectrometer from PerkinElmer was employed to obtain the Fourier transform infrared (FTIR) spectra of the samples. PHI Quantera SXM using monochromatic Al Kα with an energy of 1486.6 eV was utilized to gather information on the chemical bonding states of the fibermat for X-ray photoelectron spectroscopy (XPS). X-ray diffraction (XRD) data were collected using PANalytical Empyrean with 45 kV, 40 mA power setting, and a step size of 0.02°.

2.3. Electrochemical Measurements. The working electrodes for Na-ion half-cells were prepared with the following composition: 70 wt % of the active material (WS_2NT/SiOC fibermat), 15 wt % of carbon black as the conducting agent (Alfa Aesar, Haverhill, MA, USA), and 15 wt % of polyvinylidene fluoride (PVDF) as a binder (Alfa Aesar, Haverhill, MA, USA). A homogeneous slurry was prepared using the materials mentioned above using 1-methyl-2-pyrrolidinone (Sigma-Aldrich, Missouri, MA, USA) as a solvent for PVDF, which was added in a drop wise manner. A 9 μm thick copper substrate was coated with this slurry and dried at 80 °C for 18 h for solvent removal. The obtained film thickness was found to be 125 μm. Circular sections were obtained from this coating to be used as a working electrode for the 2032-type coin cell. The reference and counter electrodes, in this case, were prepared of sodium metal. The electrolyte used was 1.0 M $NaClO_4$ (Alfa Aesar) in (1:1 v/v) EC/DMC (anhydrous, 99%, Sigma-Aldrich), and the two electrodes were separated by a glass separator soaked with electrolytes. All the tested cells were assembled in a high precision inert (ultra-high purity Argon) atmosphere, with O_2

https://doi.org/10.1021/acsomega.2c07464
ACS Omega 2023, 8, 10126−10138

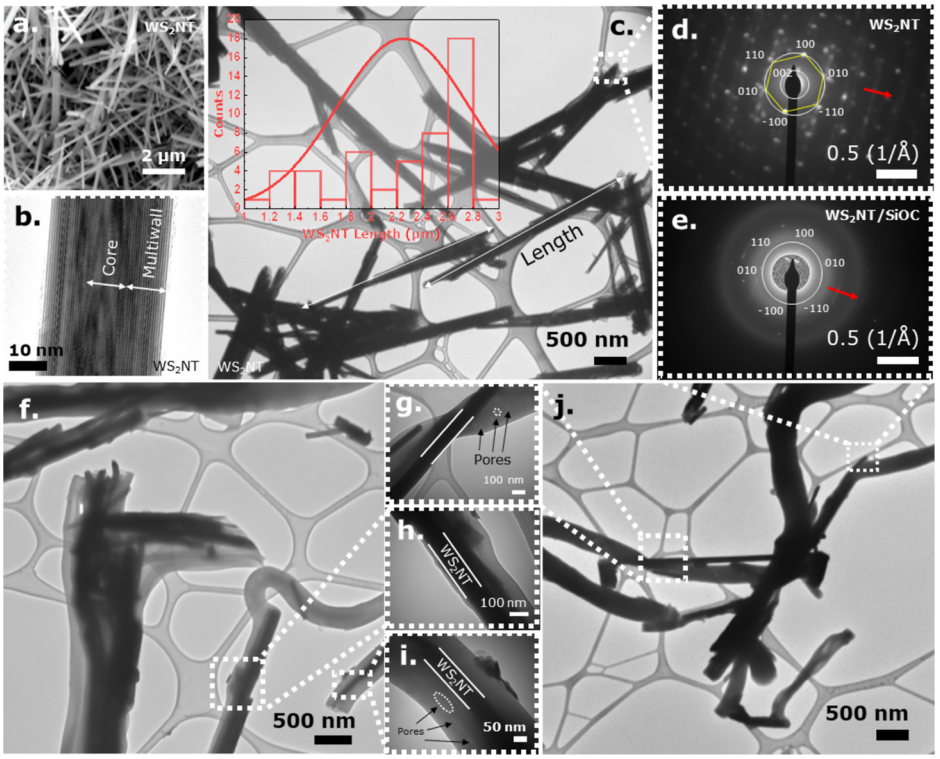

Figure 3. (a) SEM micrograph of the dense web of WS_2NTs; TEM micrograph of (b) single WS_2NT elucidating the nanotube inner and outer walls; (c) WS_2NTs elucidating the length of individual nanotubes; the insets show the distribution plot for identifying the length of individual WS_2NTs; SAED pattern of the (d) WS_2NTs showing the tube axis and crystalline nature of the nanotubes with crystal planes denoted; (e) WS_2NT/SiOC fibers where the similar hexagonal pattern of WS_2NTs was spotted along with an amorphous ring in the back; (f) TEM micrograph of the WS_2NT/SiOC fibers where the confinement of nanotubes inside the fibers could be identified; (g–i) magnified view of individual WS_2NT/SiOC fibers where the alignment of the nanotubes inside the fibers could be well specified along with the porous feature of the fibers; (j) TEM micrograph of the WS_2NTs/SiOC fibers from which a magnified view (g), and an SAED pattern (e) were obtained.

and H_2O contents below 0.1 ppm. The cycled electrodes (after 50 cycles) were de-crimped in the inert atmosphere and washed with a DMC solvent to dispose of the separators attached to the electrodes for post-cycling SEM and XPS analyses.

3. RESULTS AND DISCUSSION

3.1. Microscopic Analysis. This study utilized SEM to test the geometry of the as-produced fibermats. Morphology changes of the fibers during the as-spun, cross-linked, and pyrolyzed states were also investigated using SEM and compared to specimen weight loss during the annealing process. Figure 2a shows the fibermat immediately after electrospinning. The inset on the bottom right of the figure shows the digital camera image of the as-spun fibermat. The dark grayish color of the as-spun fibermat indicates primarily the existence of the WS_2NTs in the fibermat structure. Although occasional clumping of the fibers was observed in the fibermat (white arrows in Figure 2a,), most of the fibers were uniform in shape, as shown in the magnified view of the fibermat in Figure 2b, with only minimal irregularity. No beads were observed in the fibers from the as spun fibermats. Figure 2c,d shows the SEM micrographs of the cross-linked fibermat. The digital camera image of the fibermat in the inset of Figure 2d denoted a slight change in the color of the fibermat, indicating the vinyl polymerization state with a mass loss of 40% and fibermat (linear) shrinkage of approximately 15%. The magnified SEM figure of the cross-linked fibermat (Figure 2c) also shows minimal fiber irregularity during the cross-linking stage. In the final pyrolyzed stage, shown in Figure 2e, occasional clumps of fibers were observed. The clumps of fibers are readily visible from the magnified Figure 2f. The individual fibers in the pyrolyzed fibermat were regular in shape without beads (Figure 2g). The visual appearance of this pyrolyzed fibermat was fully black, as shown in the inset of Figure 2e. The weight loss of the final pyrolyzed WS_2NTs/SiOC fibermat from the cross-linking stage was approximately 61%, with a linear shrinkage of 50%. The fiber diameter at the as-spun, cross-linked, and post-pyrolysis stages was measured by taking an average of 25 measurements, as denoted in Figure S1a–c, respectively. A decrease in the average fiber diameter as a function of pyrolysis temperature was observed from the measurements (600–800 nm for as-spun fibers, 500–700 nm for cross-linked fibers, and 400–500 nm for pyrolyzed fibers). SEM micrographs of the pyrolyzed neat SiOC fibers are included in Figure S2(a,b), from which the difference between the neat SiOC fibers and the composite containing the WS_2NTs (Figure 2) can be well understood. The SiOC fibers were electrospun under the same electrospinning conditions but nevertheless contained irregularities in the fiber geometry with beads (shown in magnified Figure S2b). The gradual decrease in fiber diameter and weight retention of the total fibermat observed during various stages of decomposition is further investigated in spectroscopic methods. Fiber diameters in the final stage of this study correlated well with similar previous studies.[24,25] Figure 2h provides a qualitative chemical analysis of the fibermats using the energy dispersive spectroscopy (EDS) technique. The characteristic W-Lα at (8.6 keV)

https://doi.org/10.1021/acsomega.2c07464
ACS Omega 2023, 8, 10126–10138

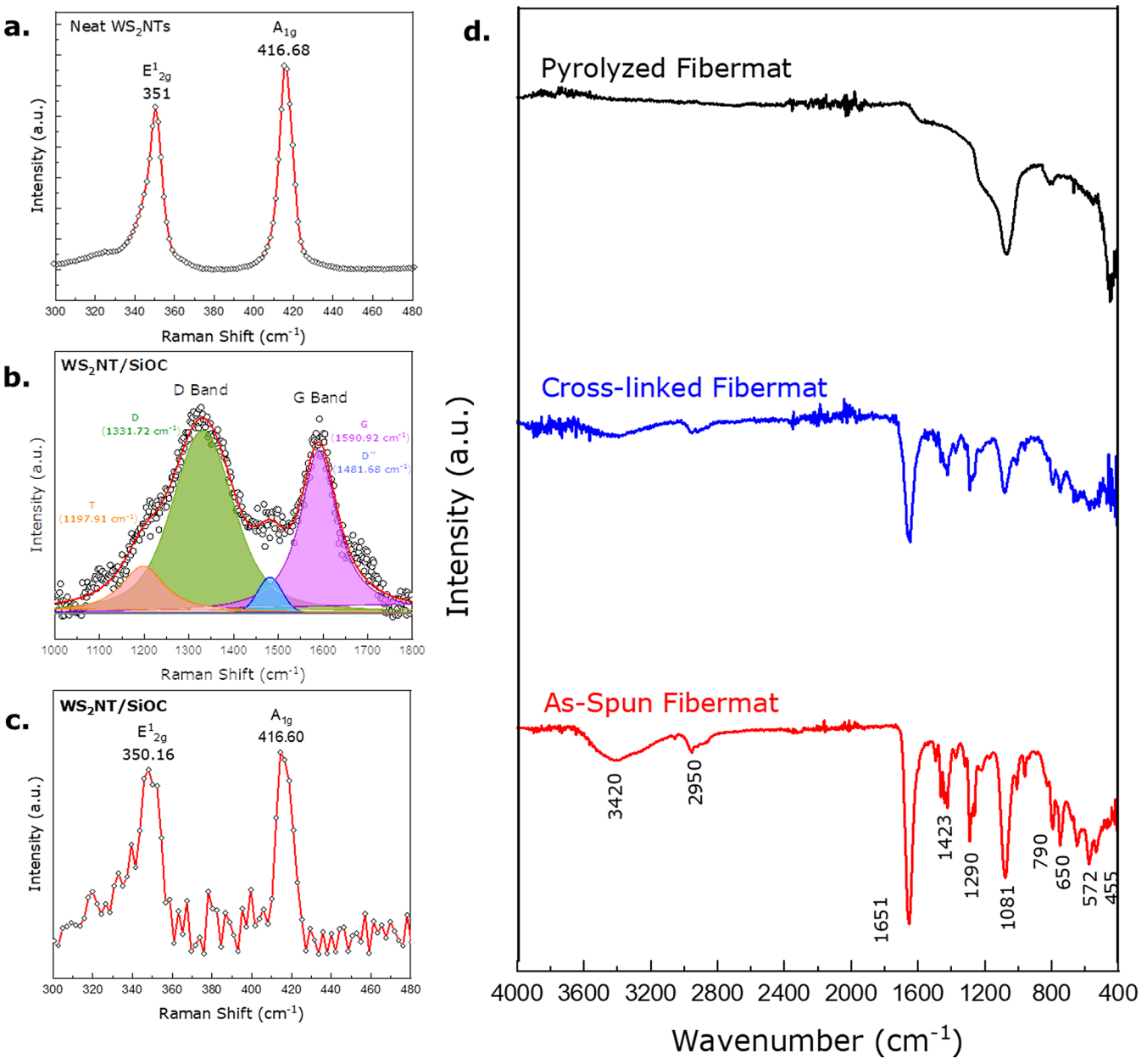

Figure 4. Raman spectra of (a) neat WS_2NTs powder showing the typical position of the peaks obtained from the neat material; (b) WS_2NT/SiOC fibermat in the higher wavenumber region confirming the free carbon species (integrated spectra using a Gaussian function); (c) WS_2NT/SiOC fibermat in the lower wavenumber region confirming the presence of the WS_2 nanotube material within the fibermat showing the same peaks as the neat material with subtle differences; (d) FTIR spectra of as-spun, cross-linked, and pyrolyzed fibermats. The spectra from top to bottom illustrate data obtained from individual pyrolyzed, cross-linked, and as-spun fibermats. The spectral analysis signifies the presence of the precursor polymer, TMD material, and PVP material in the fabricated fibermat during the cross-linking stage and after the pyrolysis step.

and S-Kα (at 2.52 keV) spectral lines were observed in the fibermat, confirming the presence of the WS_2 nanotube material. In addition, spectral lines for Si-Kα (at 1.97 keV), O-Kα (at 0.73 keV), and C-Kα (at 0.48 keV) were also observed, denoting the presence of the set of materials (W, S, Si, O, and C) that was as per expectation. Notably, the entire spectra shifted by ~0.2 keV due to calibration. Furthermore, the EDS technique resulted in an elemental distribution map of the fibermat, revealing an even distribution of the desired elements and the efficiency of the electrospinning technique as a robust fabrication method.

The SEM micrograph in Figure 3a shows a dense web of WS_2NTs. Figure 3b shows a zoomed-in view (10 nm scale) of a single multilayered nanotube with the core and the multiwall structure highlighted. The average length of the nanotubes was 1.2−2.8 μm, as determined from the resulting distribution plot included on the inset of Figure 3c. Notably, the reduction of nanotube length, which was initially reported to be 2−20 μm[23,26]—likely due to the solution preparation process for electrospinning. A selected area electron diffraction (SAED) pattern (Figure 3d) obtained from one of the nanotubes of Figure 3c (marked area in the figure) denotes the three-dimensional (3D) curvature of the crystal due to the polycrystalline-like electron diffraction pattern. The sixfold symmetrical spot pattern reflection indicates the in-plane hexagonal arrangement of atoms when WS_2 layers are

https://doi.org/10.1021/acsomega.2c07464
ACS Omega 2023, 8, 10126−10138

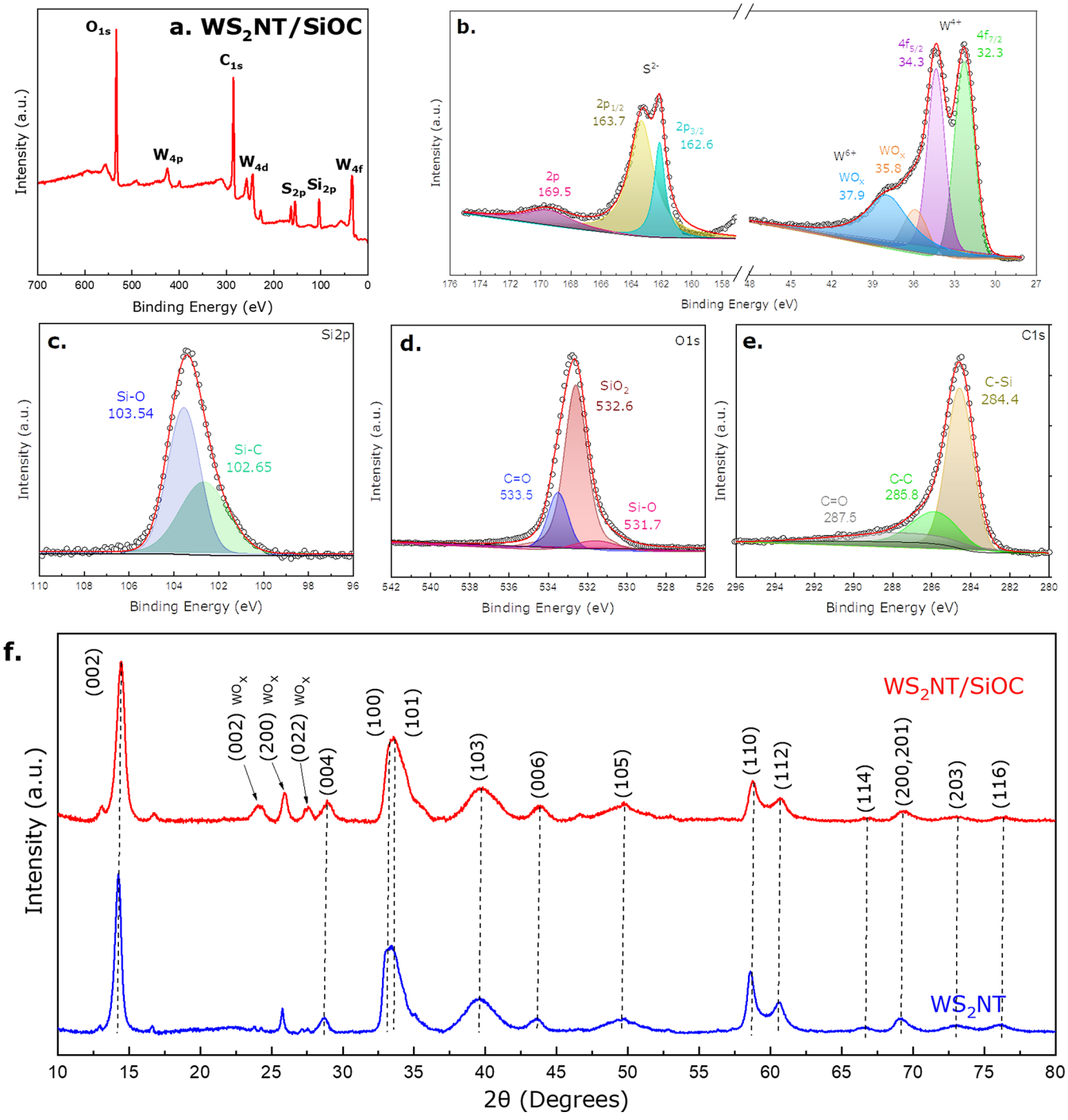

Figure 5. (a) XPS survey scan of WS_2NT/SiOC fibermats representing the presence of individual elements after pyrolysis of the fibermat at a high temperature; (b) high-resolution S 2p and W 4f XPS spectra of the WS_2NT/SiOC fibermat recording the bonding states due to s.o.s. of W and S, W being bonded with small amounts of O elevating the conductivity of the fibermat; high-resolution: (c) Si 2p XPS spectra; (d) O 1s XPS spectra; (e) C 1s XPS spectra obtained from the WS_2NT/SiOC fibermat confirming the bonding states of the Si, C, and O in the SiOC matrix; (f) comparative XRD analysis of WS_2NT (bottom pattern) and WS_2NT/SiOC (top pattern) identifying the crystalline phases of the materials within.

perpendicular to the electron beam (on the top of the tube roll). At the same time, the 002 plane denotes the vdW gap between the layers when they are parallel to the electron beam. The presence of both orientations was due to the closed nanotube structure yielding parallel and perpendicular to electron beam regions of the vdW planes. The red arrow in the image represents the axis of the nanotube, and multiple spots in the SAED pattern signify that the multiwall tubular structure was composed of multi-chiral walls that co-exist in the experimental condition. These values and conditions matched well with previous WS_2NTs studies.[25,27]

Figure 3f shows the TEM image of the WS_2NT/SiOC fibermat. The figure also confirms the state when the WS_2NTs can be confined inside the fibers. The enlarged view of this image (Figure 3g-i) reveals individual WS_2NT/SiOC fibers where the alignment of the nanotubes inside the fibers is well specified. In addition, some neat nanotubes and stacked nanotubes were confined inside the SiOC fibers, resulting in a

https://doi.org/10.1021/acsomega.2c07464
ACS Omega 2023, 8, 10126−10138

complex structure (Figure 3j). The enlarged view of the images (Figure 3g–i) also revealed the presence of some pores in the fibers. Heterostructures have been identified as a feasible solution to overcome a large volume change and subsequent poor electrical connection in TMD materials. In the heterogeneous fiber structure, the Li^+ ions can move freely along the nanotube material, and the shell of the SiOC fiber can act as a reservoir to accommodate the ions via intercalation. The flexible SiOC fiber may also buffer the volume change induced by the intercalated WS_2NTs, thereby preventing structural disintegration and maintaining a stable capacity during high-rate cycling conditions. Inevitable pores in the fibers (black arrows on Figures 3g and 3i) can be useful for maintaining the anodic performance caused by enhanced movement of the ions.[28] The SAED pattern of WS_2 nanotubes with fibers (Figure 3e) contained the same (hexagonal) spots as the neat nanotubes and the amorphous rings, proving the amorphous shape of carbons characteristic of SiOC-phase-controlling structures.

3.2. Spectroscopic Analysis. This study also used Raman spectroscopy to decipher the fibermat microstructure and designate the free-carbon phase from the SiOC fibers and the WS_2NTs materials. Figure 4a shows the Raman spectra of the neat WS_2NTs material. The two intense peaks at 351 and 416 cm^{-1} (Figure 4a) were assigned to the in-plane mode $E_{2g}{}^1$ and out-of-plane mode A_{1g}, respectively. The intensity ratio of the $E_{2g}{}^1$ peak to the A_{1g} peak for the WS_2NTs was approximately 0.91,being close to the bulk WS_2 signifying the multi-walled feature of the nanotubes (more than three layers). Additionally, the frequency difference between the two modes was approximately 65 cm^{-1}, revealing multilayer nanotubes. These values correspond well with previous studies.[29] The presence of WS_2 nanotubes in the WS_2NT/SiOC fibermat was verified by Raman spectra of 300–480 cm^{-1} with prominent $E_{2g}{}^1$ (350.161 cm^{-1}) and A_{1g} (416.58 cm^{-1}) peaks, shown in Figure 4c. The frequency difference between the two phonon modes was 66.43 cm^{-1}, which is close to the bulk material. Again, the intensity ratio of these two modes of WS_2NTs in the fibermat sample was approximately 0.91, which perfectly matched the bulk material. These two values signify that the use of 1D material in the SiOC fibermat (using this study's technique) advantageously rendered the active material in its raw state. The longitudinal acoustic phonon mode 2LA(M) mode was close to the shoulder of the $E_{2g}{}^1$ mode in the nanotube material, therefore was difficult to separate between them.[2,30] As shown in Figure 4b, the free-carbon phase of the WS_2NT/SiOC fibermat was revealed by the peak-fitted Raman spectra, with prominent D and G peaks at 1331.72 and 1590.92 cm^{-1}, respectively. Although the D peak was due to a disorder induced in the sample, the G band (E_{2g} symmetry) was responsible for the in-plane stretching of the sp^2 carbon bonds.[31] Deconvoluted Raman spectra revealed T and D″ peaks in the shoulder of D and G bands at 1197.91 and 1481.68 cm^{-1}, respectively, in which the T band signified the sp^2–sp^3 carbon–carbon double and triple bonds, and the D″ band signified the amorphous nature of the carbon in the sample as verified in TEM diffraction pattern studies.[32] The intensity ratio of the D and G bands of the fibermat was 1.1, revealing the high disorder of carbon induced in the sample.

This study also utilized FTIR to investigate the bonding complexity and interaction of the various molecules within the fiber matrix and the polymeric structure of the as-spun, cross-linked, and pyrolyzed fibermats. The bottom of Figure 4d shows the FTIR spectra of the as-spun fibermat. In general, the peaks at 1265–1285 cm^{-1} caused the –C-N bond from the PVP molecule, and the peaks in the 1650–1660 cm^{-1} region were responsible for the carbonyl group in the molecule. For the as-spun fibermat sample, strong peaks in the areas noted were visible, indicating the presence of the PVP molecule in the as-spun fibermat.[33]

The FTIR spectra also verified the facile integration of WS_2NTs with the carbon-based groups. For example, for the as-spun fibermat denoted by Figure 4d, the peaks at ∼650 and ∼1080 cm^{-1} were responsible for the W–S and S–S bonds, respectively.[34] Multiple peaks from 650 to 800 cm^{-1} highlighted the samples' C–S bonds. For example, the peak at 790 cm^{-1} was characteristic of C–S–S–C, H–C–S, and C–S bonds.[35,36] These bonds act as a proof of good adhesion between the WS_2NTs and the polymeric matrix, which enhances mechanical properties[36] and may be very important for providing electrical contact between the WS_2NTs and fibers, thereby accelerating the charge transfer. The strong absorption from 1000 to 1070 cm^{-1} indicates Si–O bonds. The presence of $-CH_3$ deformation and asymmetric stretching in Si–CH_3 bonds occurred in the ∼1261–2961 cm^{-1} region, respectively, and the absorption peak at 800 cm^{-1} indicates the Si–C stretching vibration.[37] All the analysis mentioned above confirms the presence of a preceramic polymer in the as-spun fiber morphology, which is in accordance with previous investigations[38] For the cross-linked fibermats (the curve in the middle of Figure 4d), the peak intensity decreased for both fibermat samples, indicating a polymerization reaction. Finally, Figure 4d shows the spectra of the pyrolyzed fibermats (top of the figure) with Si–O and Si–C bonds and a strong peak at 450 cm^{-1} that indicates elemental S–S bonds, ensuring the presence of S from the WS_2 molecule even after pyrolysis.

This study also utilized XPS to analyze the surface characteristics and determine the material's elements and the chemical and electronic states of the pyrolyzed sample. Figure 5a shows the XPS survey scan of the WS_2NT/SiOC fibermat, revealing the presence of W, S, Si, O, and C in the pyrolyzed fibermats with no material contamination within the instrument's sensitivity. Supporting Information Table ST1 presents the atomic percentage of the elements in the pyrolyzed fibermat. The wt % amount of W (3.1%) and S (3.4%) in the WS_2NT/SiOC fibermat showed that the WS_2 nanotube could sustain the high annealing temperature when pyrolyzed with preceramic polymer material. Moreover, the high amount of carbon in the fibermat also confirmed the free-carbon phase after the pyrolysis cycle, which was previously proven by the Raman spectroscopic analysis. Figure 5b shows high-resolution W 4f and S 2p spectra of the WS_2NT/SiOC fibermat. The Tougard function was used to subtract the background, and the spectra were fitted using the Voigt function. Spin–orbit splitting (s.o.s.) produced two core level peaks for each W 4f and S 2p, namely $4f_{7/2}$, $4f_{5/2}$, $2p_{3/2}$, and $2p_{1/2}$, respectively. For example, the binding energy of the W 4f spectra (Figure 5b on the right) showed that the W^{4+} state represented the $4f_{7/2}$ and $4f_{5/2}$ bands in 32.3 and 34.3 eV, respectively. The W spectrum also showed two peaks at binding energies of 35.8 and 37.9 eV, signifying the W^{6+} 4f state and indicating a slight amount of WO_x species in the WS_2NTs inside the SiOC fibers. Notably, this WO_x species is highly conductive and can increase the overall conductivity of the fibermat with a free-carbon state. Furthermore, two well-defined peaks in the S 2p high-resolution spectra (Figure 5b on the left) were attributed to

https://doi.org/10.1021/acsomega.2c07464
ACS Omega 2023, 8, 10126–10138

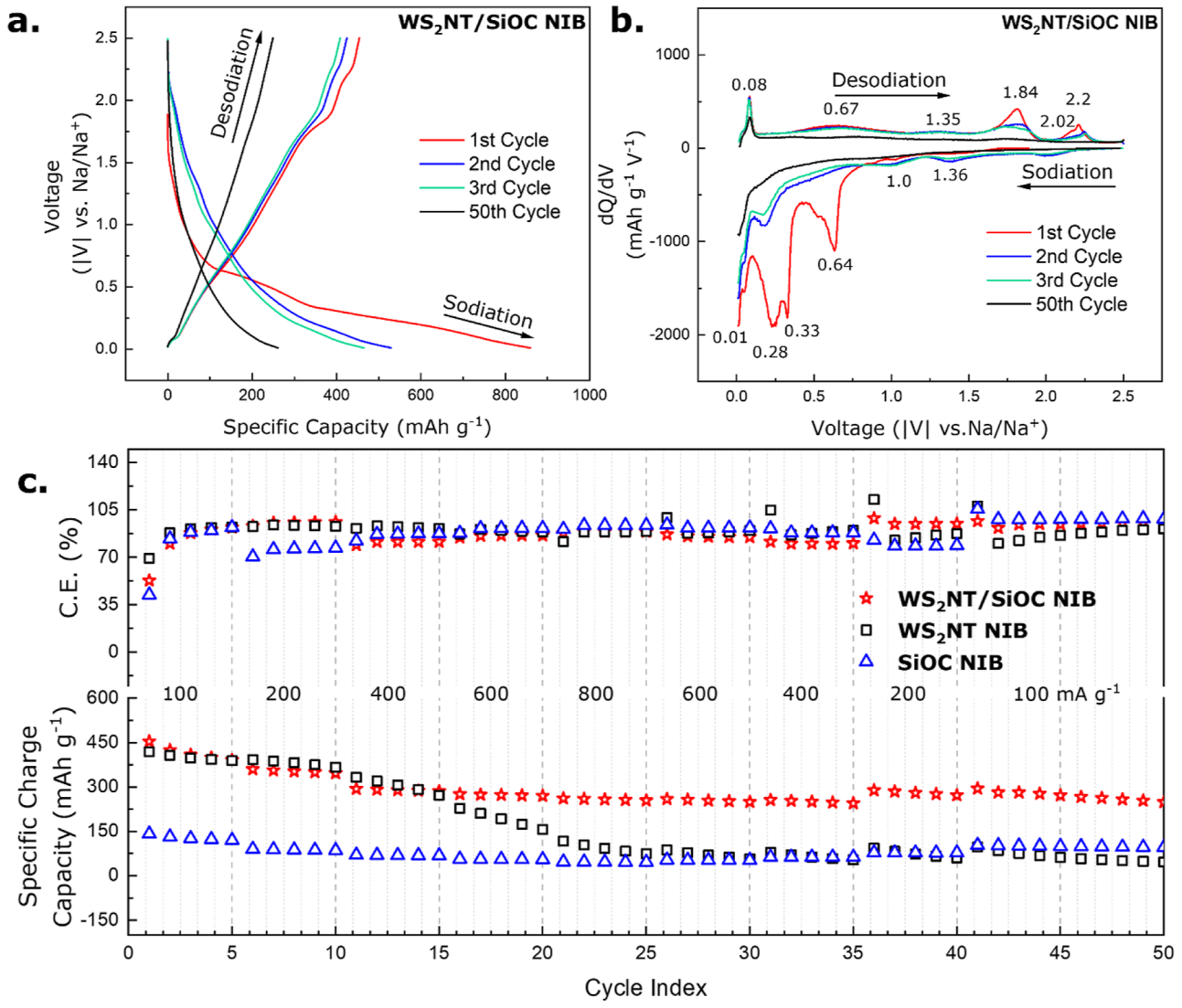

Figure 6. (a) GCD profile of the WS_2NT/SiOC composite electrode when tested in a Na-ion half-cell setup; (b) differential capacity curve of the WS_2NT/SiOC composite electrode in a Na-ion half-cell setup derived from the GCD profile, providing information regarding reactions taking place at different voltages; (c) rate capability test performed for the WS_2NT/SiOC, neat WS_2NTs, and neat SiOC electrode when tested in a Na-ion half-cell setup.

s.o.s. at 162.6 and 163.7 eV, representing $2p_{3/2}$ and $2p_{1/2}$ core levels, respectively, corresponding to S^{2-} orbitals. One more peak was observed in the S 2p high-resolution spectra in the binding energy of 169.5 eV, indicating sulfur bonded with carbon from the preceramic polymer. All these peaks agree well with previous WS_2NTs studies.[17,39] High-resolution spectra of the Si 2p, O 1s, and C 1s were also obtained for the pyrolyzed fibermat, as shown in Figure 5c−e, respectively. Deconvoluted Si 2p spectra (Figure 5c) showed Si−O and Si−C bonds in both fibermats, and the C 1s spectra in Figure 5e reveals the C−Si, C−C, and C═O bonds. The O1s spectra (Figure 5d) of both fibermats showed the Si−O, Si═O, and C═O bond states, with dominant SiO_2. The results showed that a good amount of carbon in the sample also bonded with Si, and individual SiO_2 regions were observable, thereby validating the SiOC microstructure of the pyrolyzed fibermat even after pyrolysis with WS_2 nanotubes.

XRD was utilized in this investigation for phase identification of the neat WS_2NTs and WS_2NTs within the WS_2NT/SiOC fibermat. From XRD diffractograms depicted by Figure 5f, it was apparent that the reflections from WS_2NTs and WS_2NTs/SiOC were identical. Both XRD patterns are identical because the SiOC matrix is X-ray amorphous and shows no reflections. The most prominent peak for both XRD patterns originated from the (002) crystalline plane. For the neat nanotube, the peak is located at 14.28°, which indicates a shift from the bulk WS_2 (14.32°). This shift may have originated due to the built-in strain in the nanotube lattice, further indicating that the interlayer spacing increased by a small amount.[40] A group of peaks was identified around the (002) plane for the WS_2NT/SiOC fibermat sample, which is attributed to the $W_{18}O_{49}$ phase—the intermediate precursor residuals created (from WO_3, the initial precursor) during the reduction sulfurization reaction for nanotubes' synthesis in their core.[41] Thereby, the peaks at 23.23, 24.38, and 27.15° can be attributed to (002), (200), and (022) planes of crystalline monoclinic WO_x.[42] Among the peaks mentioned above, only the (200) WO_x peak was identified for the neat WS_2NTs sample, which could be introduced during the sample preparation. For the WS_2NT/SiOC fibermat, an increase in

https://doi.org/10.1021/acsomega.2c07464
ACS Omega 2023, 8, 10126−10138

the intensity of the peaks mentioned above was also observed. The peaks of (100), (101), and (103) planes seem to be broadened, and this feature corresponds to 3D atomic positions within the WS_2NTs, originating from the network rotation along the tube axis, much like the carbon nanotubes. Peaks occurring at higher 2θ angles, such as (006), (110), (112), (114), and (116), present broad features and are indicative of the elongated periodic layered structure of the WS_2NTs. Again, the broadening of the peaks can also be correlated with the submicron size of the WS_2NTs. In summary, the identical spectra of the WS_2NTs and WS_2NT/SiOC point that SiOC functionalization of WS_2NTs does not change the crystallinity of the WS_2NTs,, and no new crystalline phases are generated during the pyrolysis process. The above-mentioned analysis corresponds well with the previous literature regarding the XRD analysis of the WS_2NTs.[43]

3.3. Electrochemical Analysis. Galvanostatic charge−discharge curves (GCD) and differential capacity curves derived from the GCD curves offered insight regarding reactions at various stages during charging and discharging cycles. Figure 6a illustrates the GCD profile, and Figure 6b illustrates the associated differential capacity curves of the WS_2NT/SiOC composite electrode. The cycling data of neat WS_2NTs, neat SiOC, and WS_2NT/SiOC composite electrodes at different current densities are represented by Figure 6c. Figure S3a depicts the GCD profile of the WS_2NTs material from which the differential capacity curve was obtained, and Figure S3b shows the material when cycled in a sodium-ion half-cell. The first sodiation step revealed only one weak peak at approximately 1.2 V due to the reversible sodium intercalation into the layers of WS_2NTs. This phenomenon can be described by the following reaction

$$x\mathrm{Na}^+ + \mathrm{WS}_2 + x\mathrm{e}^- \rightarrow \mathrm{Na}_x\mathrm{WS}_2 \quad (1)$$

Four more peaks were observed in the first cycle sodiation stage at 0.28, 0.34, 0.52, and 0.64 V due to the irreversible conversion reaction at medium (0.52 V) voltages and the formation of the solid electrolyte interface (SEI) layer, as described by the following reaction

$$4\mathrm{Na}^+ + \mathrm{WS}_2 + 4\mathrm{e}^- \rightarrow \mathrm{W} + 2\mathrm{Na}_2\mathrm{S} \quad (2)$$

The following sodiation steps revealed new peaks at 1.0, 1.36, and 2.02 V, which decreased in intensity in subsequent cycles. The peaks at 0.5 and 1.0 V indicated the occurrence of a reaction in the opposite direction as described by eq 2, while the other two peaks at 1.36 and 2.02 V were due to the multi-step extraction of sodium ions from the Na_xWS_2 matrix, as proven by previous studies of WS_2 nanowires and nano-flowers.[10,11] This electrode in this investigation was also tested in a rate capability test at an increasing current density that created a harsh cycling condition for the sodium-ion half-cell. Specifically, the increasing current density was 100, 200, 400, 600, and 800 mA g^{-1}, and the cells underwent five cycles at those current densities and then returned to initial conditions in the subsequent cycles. The first-cycle charge capacity of the electrode was 419.12 mA h g^{-1} with a coulombic efficiency of 69.28% due to irreversible reactions in the first cycle. A steep drop in capacity was recorded when the cell was returned to the initial cycling condition after high current density values, indicating low performance of the electrode in high current rates. The capacity retention of the WS_2NT electrode at the 26th, 31st, 36th, and 41st cycles was 55.95, 23.36, 21.42, and 26.6%, respectively. The low-capacity retention of the electrode was due to irreversible reactions at the electrode surface (intensification of excessive conversion reaction). This behavior correlated to the coulombic efficiency of the WS_2NT electrode not being constantly near 100% through the harsh cycling conditions, potentially indicating a structural change of the material.

Although silicon-based materials are nearly inactive in NIBs, recent investigations have found that free-carbon domains in SiOC can efficiently store Na^+ ions. Therefore, the capacity contribution of the SiOC fiber electrode potentially originates from the free-carbon domains and nanovoids. Therefore, this study investigated neat SiOC fibermats in GCD experiments at the same conditions described in Supporting Information Figure S3c. The differential capacity curve obtained from the GCD curves (Supporting Information Figure S3d) showed a pair of peaks during the sodiation/desodiation process at 0.01 and 0.09 V due to the intercalation of sodium ions in the free-carbon sites. Conversely, the peak at 0.57 V was due to the trapping of Na^+ ions into the highly active defective graphene sites, which is irreversible in the following cycles and the formation of the SEI layer, and the reversible peak at 0.67 V in the desodiation step was due to sodium intercalation into the micropores, similar to results of previous studies regarding the use of SiOC-based materials in NIB setup.[44] The first-cycle charge capacity of the SiOC electrode was 141.59 mA g^{-1} with a coulombic efficiency of 42.33%. The capacity retention of the SiOC fibermat electrode was higher than that of the WS_2NT electrode, with capacity retentions of 96.95, 92.98, 91.30, and 85.80% in the 26th, 31st, 36th, and 41st cycles, respectively. The coulombic efficiency of the SiOC fibermat electrode was also more stable than that of the WS_2NT electrode, with a slight deviation of near 100% efficiency in high current densities.

The composite WS_2NT/SiOC electrode was tested under the same conditions in a sodium-ion half-cell setup. Figure 6a is the GCD profile, while Figure 6b is the corresponding differential capacity curve for the WS_2NT/SiOC electrode. As observed in Figure 6b, in the first sodiation/desodiation step, a pair of peaks at 0.01 and 0.08 V are ascribed to sodium insertion in the disordered carbon phase and micropores present in the SiOC phase (note that these peaks were prominent in the neat SiOC electrode also) and to a lesser extent the carbon black conducting agent present in the electrode. In addition, similar to the neat WS_2NT electrode, the electrolyte decomposition and formation of the SEI layer were attributed to the peaks at 0.28, 0.33, and 0.64 V on the first sodiation step. A small peak at 0.52 V was also observed on the shoulder of the 0.64 V peak due to the conversion reaction of the WS_2NT material, indicated by eq 2. The first desodiation step resulted in peaks at 1.35, 1.84, and 2.2 V due to multi-step deintercalation in the interlayer region and into the hollow tube core of the WS_2NT material.[45] One broad peak at 0.67 V was attributed to the sodium ion's intercalation into the SiOC matrix's micropores. These peaks were reversible and decreased gradually in intensity during subsequent cycles. The first-cycle charge capacity of the composite electrode occurred at 454.05 mA h g^{-1} with a coulombic efficiency of 52.85%. Under the same rate capability conditions at the 26th, 31st, 36th, and 41st cycles, the capacity retention of the electrode was 96.1, 94, 83.39, and 75.9%, respectively, which was higher than that of the electrodes assembled with the neat WS_2NT material.

https://doi.org/10.1021/acsomega.2c07464
ACS Omega 2023, 8, 10126−10138

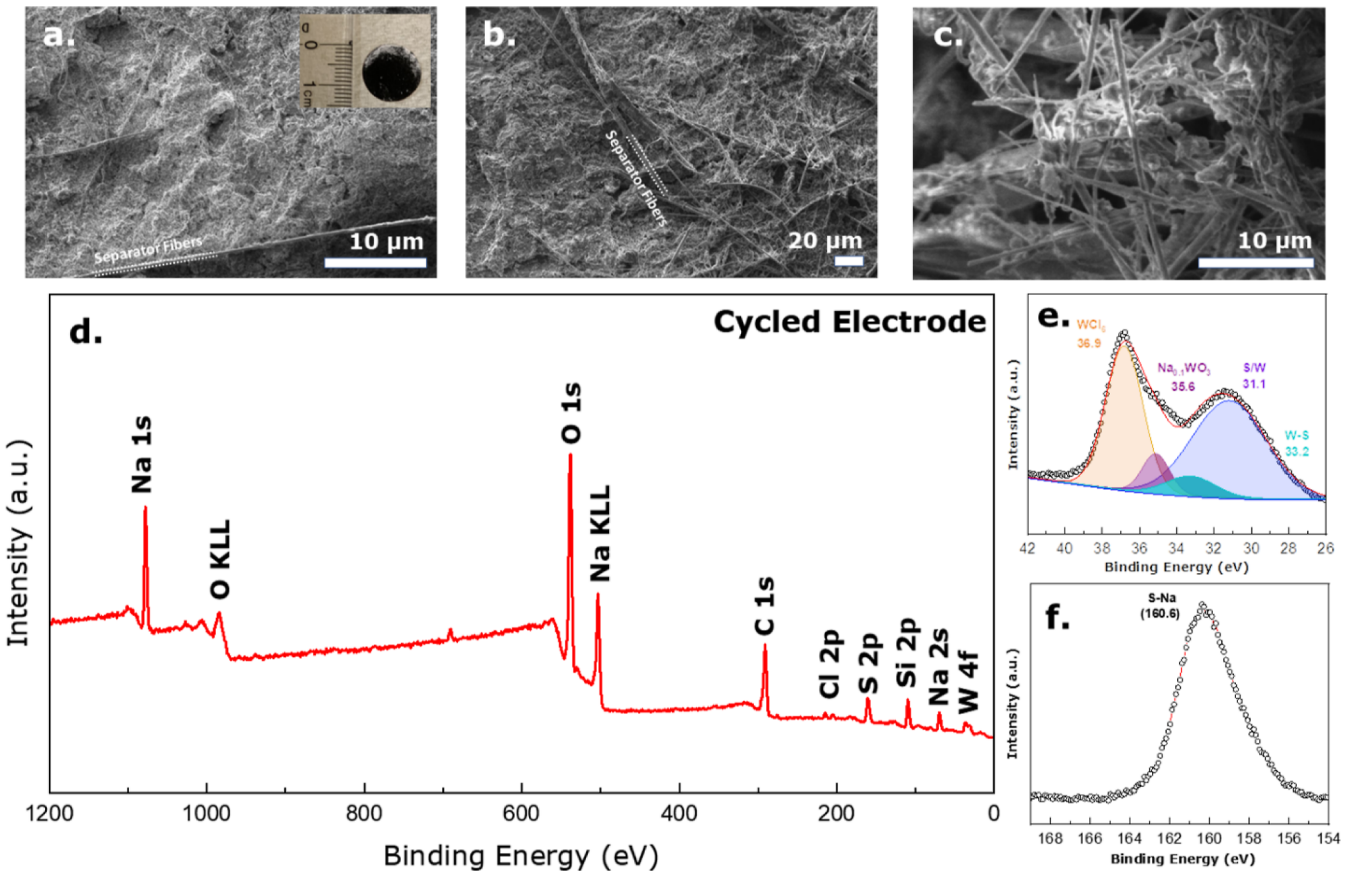

Figure 7. SEM micrograph of (a) the recovered electrode after cycling showing structural integrity, inset showing the digital camera image; (b) cycled electrode (enlarged view); (c) cycled electrode showing individual fiber geometry still intact; (d) XPS survey scan of the cycled electrode showing individual elements present within; high-resolution XPS spectra of (e) W 4f and (f) S 2p showing the chemical bonding of W and S elements.

The disassembled electrodes were further morphologically analyzed using SEM. The recovered WS_2NT/SiOC electrodes exhibit excellent retention of the fibrous network. No visible microcracks in the electrodes were found, proving the structural integrity and minimal stress development within the cycled electrodes even after cycling at harsh conditions/incrementally increasing current densities (Figure 7a,b). The digital camera image of the recovered electrode (shown on the inset of Figure 7a) showed no visible color change or physical imperfections of the spent electrode. Some white fibers from the separators of the cycled cell were visible in the digital camera image and the SEM micrographs. Figure 7c shows an enlarged view of the SEM micrographs, illustrating individual fibers from which a distribution curve extrapolated fiber diameter. The obtained average fiber diameter of the cycled electrode was between 600 and 700 nm—suggesting approximately a 40% size increase compared with the uncycled pyrolyzed fibermat (shown in Supporting Information Figure S4). The 40% increase in fiber diameter might have a minimal effect to the volume change of the whole electrode due to inter-fiber void spaces. Figure 7d shows the XPS survey scan of the recovered electrode. Along with the base materials (W, S, Si, O, and C), Cl and Na (high percentage, 20.47 wt %) were present, indicating the formation of the SEI layer. Table ST2 in the Supporting Information section shows the elemental composition of the spent electrode obtained from the XPS spectra. The preservation in the wt % ratio of W and S elements (W = 4.17 wt %, S = 4.69 wt %) compared to the WS_2/SiOC pyrolyzed fibermat suggests the safeguarding effect of SiOC fibers toward WS_2NTs. Figure 7e,f shows the high-resolution XPS spectra of the W4f and S2p plots, respectively. W 4f spectra were deconvoluted into four individual peaks: WCl_6 (36.9 eV), $Na_{0.1}WO_3$ (35.6 eV), S/W (31.1 eV), and W−S (33.2 eV),[46−49] stipulating the undergoing reaction and formation of the SEI layer. On the other hand, only the S−Na (160.6 eV) bond was present in the S 2p spectra—most likely arising from a conversion-type reaction with Na ions.[50]

The synergistic effect of the composite electrode was evident from the differential capacity curve, in which the peaks associated with SEI layer formation and conversion reaction of the WS_2NT electrode decreased in intensity for the composite electrode. Since all the cells were synthesized, assembled, and tested under identical conditions, the assumption was that SiOC prevented such conversion reactions and provided additional storage sites for the material. In addition, because SiOC is amorphous and does not chemically bond with WS_2NTs, as shown via spectroscopic and microscopic analyses, the structure of the neat material (WS_2NTs) did not change. The SiOC material also potentially prevented the agglomeration of TMDs and the dissolution of polysulfides into the electrolyte, as evidenced by the increased capacity retention at high current densities. When the current density returned to the initial values of 600, 400, 200, and 100 mA g^{-1}, the recovered capacity was 259.38, 256.04, 289.07, and 294.94 mA h g^{-1}, respectively. The capacity values of the composite WS_2NT/SiOC electrode in the cycles mentioned above were

https://doi.org/10.1021/acsomega.2c07464
ACS Omega 2023, 8, 10126−10138

2.96, 4.02, 3.68, and 2.85 times higher, respectively, than the capacities of the half-cell assembled with the WS_2NT electrode in the same cycles. The superior performance of the WS_2NT/SiOC electrode (due to the SiOC matrix, which induces stable cycling of Na^+ ions) compared to similar TMD-based composite electrodes is illustrated in Table ST3. Therefore, the composite electrode's symbiotic behavior reinforces the claim that the SiOC functionalization of the active sulfur-based TMDs in appropriate proportions may prevent polysulfide dissolution in an electrochemical cell.

4. CONCLUSIONS

This is the first work to study WS_2NTs confined within SiOC fibers to form a heterogeneous structure that provides stable cycling performance in high current densities in a Na^+-ion half-cell configuration. The hybrid composite structure was achieved via single-step electrospinning followed by pyrolysis at elevated temperatures. Microscopic (SEM and TEM) and spectroscopic (Raman, FTIR, and XPS) techniques were utilized to identify materials within the heterostructure, the materials' chemical bonding states, the evolution of the fibrous structure during various annealing stages, and the existence of the free-carbon domain within the SiOC fibers. The crystallinity of the WS_2NTs was well preserved within the heterostructure (proven by XRD and SAED analyses), confirming the facile chemical functionalization of the nanotubes. When tested in a sodium-ion half-cell, the composite electrode showed increased stability at high current densities and robust capacity retention (approximately 2−3 times higher than the capacity of the neat WS_2NTs) at subsequent cycles. The improved electrochemical performance of the heterostructure with the post-cycle analysis of the electrode confirms the authors' initial hypothesis that the SiOC fibers might protect the WS_2NTs from negative occurrences to an extent, such as capacity degradation, volume expansion, irreversible conversion reaction, and polysulfide dissolution, and contribute to the fabrication of better-performing electrodes for room temperature NIBs.

■ ASSOCIATED CONTENT

Supporting Information

The Supporting Information is available free of charge at https://pubs.acs.org/doi/10.1021/acsomega.2c07464.

Data of fiber diameter distribution, SEM micrographs of SiOC pyrolyzed fibers, XPS elemental composition of the fibermat, GCD profile and differential capacity curves of WS_2NT and SiOC fibermats in an NIB half-cell, fiber data distribution of the spent electrode, the elemental composition of the cycled electrode, and summary and comparison of electrode performance (PDF)

■ AUTHOR INFORMATION

Corresponding Author

Gurpreet Singh − *Department of Mechanical and Nuclear Engineering, Kansas State University, Manhattan, Kansas 66506, United States*; Email: gurpreet@ksu.edu

Authors

Sonjoy Dey − *Department of Mechanical and Nuclear Engineering, Kansas State University, Manhattan, Kansas 66506, United States*; orcid.org/0000-0001-6244-2750

Krishnappa Manjunath − *Faculty of Sciences, Holon Institute of Technology, Holon 5810201, Israel*

Alla Zak − *Faculty of Sciences, Holon Institute of Technology, Holon 5810201, Israel*; orcid.org/0000-0002-3807-3454

Complete contact information is available at: https://pubs.acs.org/10.1021/acsomega.2c07464

Author Contributions

Conceptualization: G.S.; methodology: G.S. and S.D.; WS_2NT synthesis and TEM analysis: A.Z.; SEM, XPS, Raman, FTIR, and XRD analyses: S.D.; investigation: S.D.; SEM analysis: K.M.; resources: G.S.; data curation: S.D.; writing-original draft preparation: S.D.; writing-review and editing: G.S.; editing: A.Z.; visualization: S.D.; supervision: G.S.; funding acquisition: G.S. All authors have read and agreed to the published version of the manuscript.

Funding

This work is supported by the National Science Foundation grants #1743701, 1454151, and 2025298.

Notes

The authors declare no competing financial interest.

■ ACKNOWLEDGMENTS

Financial support from the National Science Foundation (NSF) Partnerships for International Research and Education (PIRE) is gratefully acknowledged. A.Z. thankful to "Science for Peace and Security (SPS) Programme of NATO" for financial support. The authors thank Davi Marcelo Soares for his help in developing the electrospinning setup. The research was performed in part in the Nebraska Nanoscale Facility: National Nanotechnology Coordinated Infrastructure and the Nebraska Center for Materials and Nanoscience (and/or NERCF), which are supported by the National Science Foundation and the Nebraska Research Initiative. G.S. and S.D. thank professor Reshef Tenne, Weizmann Institute of Science, for introducing them to A.Z. The authors would also like to acknowledge useful discussion regarding the preparation of manuscript from Dr. Reshef Tenne.

■ REFERENCES

(1) Li, Y.; Zhang, J.; Chen, Q.; Xia, X.; Chen, M. Emerging of Heterostructure Materials in Energy Storage: A Review. *Adv. Mater.* **2021**, *33*, 2100855.

(2) Viršek, M.; Jesih, A.; Milošević, I.; Damnjanović, M.; Remškar, M. Raman scattering of the MoS_2 and WS_2 single nanotubes. *Surf. Sci.* **2007**, *601*, 2868−2872.

(3) Tenne, R. Advances in the Synthesis of Inorganic Nanotubes and Fullerene-Like Nanoparticles. *Angew. Chem., Int. Ed.* **2003**, *42*, 5124−5132.

(4) Chhowalla, M.; Shin, H. S.; Eda, G.; Li, L.-J.; Loh, K. P.; Zhang, H. The chemistry of two-dimensional layered transition metal dichalcogenide nanosheets. *Nat. Chem.* **2013**, *5*, 263−275.

(5) Ghosh, S.; Qi, Z.; Wang, H.; Martha, S. K.; Pol, V. G. WS_2 anode in Na and K-ion battery: Effect of upper cut-off potential on electrochemical performance. *Electrochim. Acta* **2021**, *383*, 138339.

(6) Feng, C.; Huang, L.; Guo, Z.; Liu, H. Synthesis of tungsten disulfide (WS_2) nanoflakes for lithium ion battery application. *Electrochem. Commun.* **2007**, *9*, 119−122.

(7) Lei, T.; Chen, W.; Huang, J.; Yan, C.; Sun, H.; Wang, C.; Zhang, W.; Li, Y.; Xiong, J. Multi-Functional Layered WS2Nanosheets for Enhancing the Performance of Lithium-Sulfur Batteries. *Adv. Energy Mater.* **2017**, *7*, 1601843.

(8) Song, Y.; Liao, J.; Chen, C.; Yang, J.; Chen, J.; Gong, F.; Wang, S.; Xu, Z.; Wu, M. Controllable morphologies and electrochemical

performances of self-assembled nano-honeycomb WS_2 anodes modified by graphene doping for lithium and sodium ion batteries. *Carbon* **2019**, *142*, 697−706.
(9) Wang, G. X.; Bewlay, S.; Yao, J.; Liu, H. K.; Dou, S. X. Tungsten Disulfide Nanotubes for Lithium Storage. *Electrochem. Solid-State Lett.* **2004**, *7*, A321.
(10) Li, X.; Zhang, J.; Liu, Z.; Fu, C.; Niu, C. WS_2 nanoflowers on carbon nanotube vines with enhanced electrochemical performances for lithium and sodium-ion batteries. *J. Alloys Compd.* **2018**, *766*, 656−662.
(11) Liu, Y.; Zhang, N.; Kang, H.; Shang, M.; Jiao, L.; Chen, J. WS_2 Nanowires as a High-Performance Anode for Sodium-Ion Batteries. *Chem.—Eur. J.* **2015**, *21*, 11878−11884.
(12) Wang, J.; Yu, L.; Zhou, Z.; Zeng, L.; Wei, M. Template-free synthesis of metallic WS_2 hollow microspheres as an anode for the sodium-ion battery. *J. Colloid Interface Sci.* **2019**, *557*, 722−728.
(13) (a) Remskar, M.; Mrzel, A.; Virsek, M.; Godec, M.; Krause, M.; Kolitsch, A.; Singh, A.; Seabaugh, A. The MoS_2 Nanotubes with Defect-Controlled Electric Properties. *Nanoscale Res. Lett.* **2010**, *6*, 26. (b) Yu, B.; Chen, Y.; Wang, Z.; Chen, D.; Wang, X.; Zhang, W.; He, J.; He, W. 1T-MoS_2 nanotubes wrapped with N-doped graphene as highly-efficient absorbent and electrocatalyst for Li-S batteries. *J. Power Sources* **2020**, *447*, 227364. (c) Chen, J.; Kuriyama, N.; Yuan, H.; Takeshita, H. T.; Sakai, T. Electrochemical Hydrogen Storage in MoS_2 Nanotubes. *J. Am. Chem. Soc.* **2001**, *123*, 11813−11814. (d) Liu, Y.; He, X.; Hanlon, D.; Harvey, A.; Khan, U.; Li, Y.; Coleman, J. N. Electrical, Mechanical, and Capacity Percolation Leads to High-Performance MoS_2/Nanotube Composite Lithium Ion Battery Electrodes. *ACS Nano* **2016**, *10*, 5980−5990. (e) Wei, S.; Serra, M.; Mourdikoudis, S.; Zhou, H.; Wu, B.; Děkanovský, L.; Šturala, J.; Luxa, J.; Tenne, R.; Zak, A.; et al. Improved Electrochemical Performance of NTs-WS_2@C Nanocomposites for Lithium-Ion and Sodium-Ion Batteries. *ACS Appl. Mater. Interfaces* **2022**, *14*, 46386−46400. (f) Woo, S. H.; Yadgarov, L.; Rosentsveig, R.; Park, Y.; Song, D.; Tenne, R.; Hong, S. Y. Fullerene-like Re-Doped MoS_2 Nanoparticles as an Intercalation Host with Fast Kinetics for Sodium Ion Batteries. *Isr. J. Chem.* **2015**, *55*, 599−603.
(14) Wang, Y.; Ma, Z.; Chen, Y.; Zou, M.; Yousaf, M.; Yang, Y.; Yang, L.; Cao, A.; Han, R. P. S. Controlled Synthesis of Core-Shell Carbon@MoS_2 Nanotube Sponges as High-Performance Battery Electrodes. *Adv. Mater.* **2016**, *28*, 10175−10181.
(15) Ghorbani-Asl, M.; Zibouche, N.; Wahiduzzaman, M.; Oliveira, A. F.; Kuc, A.; Heine, T. Electromechanics in MoS_2 and WS_2: nanotubes vs. monolayers. *Sci. Rep.* **2013**, *3*, 2961.
(16) (a) Piskunov, S.; Lisovski, O.; Zhukovskii, Y. F.; D'yachkov, P. N.; Evarestov, R. A.; Kenmoe, S.; Spohr, E. First-Principles Evaluation of the Morphology of WS_2 Nanotubes for Application as Visible-Light-Driven Water-Splitting Photocatalysts. *ACS Omega* **2019**, *4*, 1434−1442. (b) Evarestov, R. A.; Bandura, A. V.; Porsev, V. V.; Kovalenko, A. V. Phonon spectra, electronic, and thermodynamic properties of WS_2 nanotubes. *J. Comput. Chem.* **2017**, *38*, 2581−2593. (c) Tal, O.; Remskar, M.; Tenne, R.; Haase, G. The effect of substrate topography on the local electronic structure of WS_2 nanotubes. *Chem. Phys. Lett.* **2001**, *344*, 434−440. (d) Guo, D.; Yang, K.; Zhang, C.-X.; Shen, T.; Deng, H.-X. Electronic structures and band alignment transition in double-wall MoS_2/WS_2 nanotubes for optoelectronic applications. *J. Phys. D: Appl. Phys.* **2021**, *54*, 095105.
(17) Grillo, A.; Passacantando, M.; Zak, A.; Pelella, A.; Di Bartolomeo, A. WS 2 Nanotubes: Electrical Conduction and Field Emission Under Electron Irradiation and Mechanical Stress. *Small* **2020**, *16*, 2002880.
(18) Ghosh, S.; Brüser, V.; Kaplan-Ashiri, I.; Popovitz-Biro, R.; Peglow, S.; Martínez, J. I.; Alonso, J. A.; Zak, A. Cathodoluminescence in single and multiwall WS_2 nanotubes: Evidence for quantum confinement and strain effect. *Appl. Phys. Rev.* **2020**, *7*, 041401.
(19) Soares, D. M.; Mukherjee, S.; Singh, G. TMDs beyond MoS_2 for Electrochemical Energy Storage. *Chem.—Eur. J.* **2020**, *26*, 6320−6341.
(20) Yun, Q.; Lu, Q.; Zhang, X.; Tan, C.; Zhang, H. Three-Dimensional Architectures Constructed from Transition-Metal Dichalcogenide Nanomaterials for Electrochemical Energy Storage and Conversion. *Angew. Chem., Int. Ed.* **2018**, *57*, 626−646.
(21) Wei, S.; Serra, M.; Mourdikoudis, S.; Zhou, H.; Wu, B.; Děkanovský, L.; Šturala, J.; Luxa, J.; Tenne, R.; Zak, A.; et al. Improved Electrochemical Performance of NTs-WS_2@C Nanocomposites for Lithium-Ion and Sodium-Ion Batteries. *ACS Appl. Mater. Interfaces* **2022**, *14*, 46386.
(22) (a) Mukherjee, S.; Ren, Z.; Singh, G. Molecular polymer-derived ceramics for applications in electrochemical energy storage devices. *J. Phys. D: Appl. Phys.* **2018**, *51*, 463001. (b) Soares, D. M.; Singh, G. SiOC functionalization of MoS_2 as a means to improve stability as sodium-ion battery anode. *Nanotechnology* **2020**, *31*, 145403.
(23) Chithaiah, P.; Ghosh, S.; Idelevich, A.; Rovinsky, L.; Livneh, T.; Zak, A. Solving the "MoS_2 Nanotubes" Synthetic Enigma and Elucidating the Route for Their Catalyst-Free and Scalable Production. *ACS Nano* **2020**, *14*, 3004−3016.
(24) (a) Dey, S. Enhanced Li-Ion Rate Capability and Stable Efficiency Enabled by $MoSe_2$ Nanosheets in Polymer-Derived Silicon Oxycarbide Fiber Electrodes. *Nanomaterials* **2022**, *12*, 553. (b) Ren, Z.; Gervais, C.; Singh, G. Fabrication and characterization of silicon oxycarbide fibre-mats via electrospinning for high temperature applications. *RSC Adv.* **2020**, *10*, 38446−38455.
(25) Wang, M.; Fang, D.; Wang, N.; Jiang, S.; Nie, J.; Yu, Q.; Ma, G. Preparation of PVDF/PVP core-shell nanofibers mats via homogeneous electrospinning. *Polymer* **2014**, *55*, 2188−2196.
(26) Rothschild, A.; Popovitz-Biro, R.; Lourie, O.; Tenne, R. Morphology of Multiwall WS2 Nanotubes. *J. Phys. Chem. B* **2000**, *104*, 8976−8981.
(27) (a) Tenne, R.; Margulis, L.; Genut, M.; Hodes, G. Polyhedral and cylindrical structures of tungsten disulphide. *Nature* **1992**, *360*, 444−446. (b) Qin, F.; Shi, W.; Ideue, T.; Yoshida, M.; Zak, A.; Tenne, R.; Kikitsu, T.; Inoue, D.; Hashizume, D.; Iwasa, Y. Superconductivity in a chiral nanotube. *Nat. Commun.* **2017**, *8*, 14465.
(28) Lee, B.-S.; Son, S.-B.; Park, K.-M.; Lee, G.; Oh, K. H.; Lee, S.-H.; Yu, W.-R. Effect of Pores in Hollow Carbon Nanofibers on Their Negative Electrode Properties for a Lithium Rechargeable Battery. *ACS Appl. Mater. Interfaces* **2012**, *4*, 6702−6710.
(29) (a) Berkdemir, A.; Gutiérrez, H. R.; Botello-Méndez, A. R.; Perea-López, N.; Elías, A. L.; Chia, C.-I.; Wang, B.; Crespi, V. H.; López-Urías, F.; Charlier, J.-C.; et al. Identification of individual and few layers of WS2 using Raman Spectroscopy. *Sci. Rep.* **2013**, *3*, 1755. (b) Zeng, H.; Liu, G.-B.; Dai, J.; Yan, Y.; Zhu, B.; He, R.; Xie, L.; Xu, S.; Chen, X.; Yao, W.; et al. Optical signature of symmetry variations and spin-valley coupling in atomically thin tungsten dichalcogenides. *Sci. Rep.* **2013**, *3*, 1608.
(30) (a) Wang, X. H.; Zheng, C. C.; Ning, J. Q. Influence of curvature strain and Van der Waals force on the inter-layer vibration mode of WS2 nanotubes: A confocal micro-Raman spectroscopic study. *Sci. Rep.* **2016**, *6*, 33091. (b) Staiger, M.; Rafailov, P.; Gartsman, K.; Telg, H.; Krause, M.; Radovsky, G.; Zak, A.; Thomsen, C. Excitonic resonances in WS2nanotubes. *Phys. Rev. B: Condens. Matter Mater. Phys.* **2012**, *86*, 165423.
(31) (a) Rosenburg, F.; Ionescu, E.; Nicoloso, N.; Riedel, R. High-Temperature Raman Spectroscopy of Nano-Crystalline Carbon in Silicon Oxycarbide. *Materials* **2018**, *11*, 93. (b) Bokobza, L.; Bruneel, J.-L.; Couzi, M. Raman Spectra of Carbon-Based Materials (from Graphite to Carbon Black) and of Some Silicone Composites. *C* **2015**, *1*, 77−94.
(32) Mera, G.; Navrotsky, A.; Sen, S.; Kleebe, H.-J.; Riedel, R. Polymer-derived SiCN and SiOC ceramics - structure and energetics at the nanoscale. *J. Mater. Chem. A* **2013**, *1*, 3826−3836.
(33) Bryaskova, R.; Pencheva, D.; Nikolov, S.; Kantardjiev, T. Synthesis and comparative study on the antimicrobial activity of hybrid materials based on silver nanoparticles (AgNps) stabilized by polyvinylpyrrolidone (PVP). *J. Chem. Biol.* **2011**, *4*, 185.

https://doi.org/10.1021/acsomega.2c07464
ACS Omega 2023, 8, 10126−10138

(34) Coates, J. Interpretation of Infrared Spectra, A Practical Approach; *Encyclopedia of Analytical Chemistry*; John Wiley & Sons Ltd, 2006.
(35) (a) Hampton, C.; Demoin, D.; Glaser, R. E. *Vibrational Spectroscopy Tutorial: Sulfur and Phosphorus*; Fall 2010 Organic Spectroscopy; University of Missouri, 2010 (b) Ben Ishay, R.; Harel, Y.; Lavi, R.; Lellouche, J.-P. Multiple functionalization of tungsten disulfide inorganic nanotubes by covalently grafted conductive polythiophenes. *RSC Adv.* **2016**, *6*, 89585−89598.
(36) Shneider, M.; Dodiuk, H.; Kenig, S.; Tenne, R. The Effect of Tungsten Sulfide Fullerene-Like Nanoparticles on the Toughness of Epoxy Adhesives. *J. Adhes. Sci. Technol.* **2010**, *24*, 1083−1095.
(37) Graczyk-Zajac, M.; Vrankovic, D.; Waleska, P.; Hess, C.; Sasikumar, P. V.; Lauterbach, S.; Kleebe, H.-J.; Sorarù, G. D. The Li-storage capacity of SiOC glasses with and without mixed silicon oxycarbide bonds. *J. Mater. Chem. A* **2018**, *6*, 93−103.
(38) (a) Huang, K.; Elsayed, H.; Franchin, G.; Colombo, P. Complex SiOC ceramics from 2D structures by 3D printing and origami. *Addit. Manuf.* **2020**, *33*, 101144. (b) Liu, C.; Meng, X.; Zhang, X.; Hong, C.; Han, J.; Han, W.; Xu, B.; Dong, S.; Du, S. High temperature structure evolution of macroporous SiOC ceramics prepared by a sol−gel method. *Ceram. Int.* **2015**, *41*, 11091−11096.
(39) (a) Riga, J.; Snauwaert, P.; De Pryck, A.; Lazzaroni, R.; Boutique, J. P.; Verbist, J. J.; Brédas, J. L.; André, J. M.; Taliani, C. Electronic structure of sulphur-containing conducting polymers. *Synth. Met.* **1987**, *21*, 223−228. (b) Nethravathi, C.; Jeffery, A. A.; Rajamathi, M.; Kawamoto, N.; Tenne, R.; Golberg, D.; Bando, Y. Chemical Unzipping of WS2 Nanotubes. *ACS Nano* **2013**, *7*, 7311−7317. (c) Sedova, A.; Višić, B.; Vega-Mayoral, V.; Vella, D.; Gadermaier, C.; Dodiuk, H.; Kenig, S.; Tenne, R.; Gvishi, R.; Bar, G. Silica aerogels as hosting matrices for WS2 nanotubes and their optical characterization. *J. Mater. Sci.* **2020**, *55*, 7612−7623. (d) Seo, B.; Jeong, H. Y.; Hong, S. Y.; Zak, A.; Joo, S. H. Impact of a conductive oxide core in tungsten sulfide-based nanostructures on the hydrogen evolution reaction. *Chem. Commun.* **2015**, *51*, 8334−8337. (e) Chen, R.; Zhao, T.; Wu, W.; Wu, F.; Li, L.; Qian, J.; Xu, R.; Wu, H.; Albishri, H. M.; Al-Bogami, A. S.; et al. Free-Standing Hierarchically Sandwich-Type Tungsten Disulfide Nanotubes/Graphene Anode for Lithium-Ion Batteries. *Nano Lett.* **2014**, *14*, 5899−5904.
(40) Zak, A.; Sallacan-Ecker, L.; Margolin, A.; Feldman, Y.; Popovitz-Biro, R.; Albu-Yaron, A.; Genut, M.; Tenne, R. Scaling Up of the WS2Nanotubes Synthesis. *Fullerenes, Nanotub. Carbon Nanostruct.* **2010**, *19*, 18−26.
(41) Zak, A.; Sallacan-ecker, L.; Margolin, A.; Genut, M.; Tenne, R. INSIGHT INTO THE GROWTH MECHANISM OF WS2 NANOTUBES IN THE SCALED-UP FLUIDIZED-BED REACTOR. *Nano* **2009**, *04*, 91−98.
(42) Fu, L.; Xia, T.; Zheng, Y.; Yang, J.; Wang, A.; Wang, Z. Preparation of WO3-reduced graphene oxide nanocomposites with enhanced photocatalytic property. *Ceram. Int.* **2015**, *41*, 5903.
(43) (a) Magee, E.; Tang, F.; Ozdemir, E.; Walker, M.; Di Luccio, T.; Kornfield, J. A.; Zak, A.; Tenne, R.; McNally, T. WS2 Nanotubes as a 1D Functional Filler for Melt Mixing with Poly(lactic acid):Implications for Composites Manufacture. *ACS Appl. Nano Mater.* **2022**, *5*, 6385−6397. (b) Sinha, S. S.; Yadgarov, L.; Aliev, S. B.; Feldman, Y.; Pinkas, I.; Chithaiah, P.; Ghosh, S.; Idelevich, A.; Zak, A.; Tenne, R. MoS2 and WS2 Nanotubes: Synthesis, Structural Elucidation, and Optical Characterization. *J. Phys. Chem. C* **2021**, *125*, 6324−6340. (c) Zhu, Y. Q.; Hsu, W. K.; Terrones, H.; Grobert, N.; Chang, B. H.; Terrones, M.; Wei, B. Q.; Kroto, H. W.; Walton, D. R. M.; Boothroyd, C. B.; et al. Morphology, structure and growth of WS2 nanotubes. *J. Mater. Chem.* **2000**, *10*, 2570−2577.
(44) (a) Kaspar, J.; Storch, M.; Schitco, C.; Riedel, R.; Graczyk-Zajac, M. SiOC(N)/Hard Carbon Composite Anodes for Na-Ion Batteries: Influence of Morphology on the Electrochemical Properties. *J. Electrochem. Soc.* **2015**, *163*, A156−A162. (b) Kim, D.; Kim, H.; Lim, H.; Kim, K. J.; Jung, H.-G.; Byun, D.; Kim, C.; Choi, W. A facile control in free-carbon domain with divinylbenzene for the high-rate-performing Sb/ SiOC composite anode material in sodium-ion batteries. *Int. J. Energy Res.* **2020**, *44*, 11473−11486.
(45) Zak, A.; Feldman, Y.; Lyakhovitskaya, V.; Leitus, G.; Popovitz-Biro, R.; Wachtel, E.; Cohen, H.; Reich, S.; Tenne, R. Alkali Metal Intercalated Fullerene-Like MS2 (M = W, Mo) Nanoparticles and Their Properties. *J. Am. Chem. Soc.* **2002**, *124*, 4747−4758.
(46) Jaegermann, W.; Ohuchi, F. S.; Parkinson, B. A. Interaction of Cu, Ag and Au with van der Waals faces of WS, and SnS2. *Surf. Sci.* **1988**, *201*, 211−227.
(47) Mullins, D. R.; Lyman, P. F. Sulfur-induced changes in the W(001) surface core level shift. *Surf. Sci. Lett.* **1993**, *285*, L473−L478.
(48) Biloen, P.; Pott, G. T. X-ray photoelectron spectroscopy study of supported tungsten oxide. *J. Catal.* **1973**, *30*, 169−174.
(49) McGuire, G.; Schweitzer, G. K.; Carlson, T. A. Core electron binding energies in some Group IIIA, VB, and VIB compounds. *Inorg. Chem.* **1973**, *12*, 2450−2453.
(50) David, L.; Bhandavat, R.; Singh, G. MoS_2/Graphene Composite Paper for Sodium-Ion Battery Electrodes. *ACS Nano* **2014**, *8*, 1759−1770.

https://doi.org/10.1021/acsomega.2c07464
ACS Omega 2023, 8, 10126−10138